

Beam induced vacuum effects in the future circular hadron collider beam vacuum chamber

I. Bellafont,^{1,2} L. Mether^{ⓧ,3,2}, R. Kersevan,² O. B. Malyshev^{ⓧ,4}, V. Baglin^{ⓧ,2},
P. Chigiato,² and F. Pérez¹

¹*ALBA Synchrotron Light Source, 08290 Cerdanyola del Vallès, Spain*

²*CERN, The European Organization for Nuclear Research, CH-1211 Geneva, Switzerland*

³*EPFL, Ecole Polytechnique Fédérale de Lausanne, CH-1015 Lausanne, Switzerland*

⁴*ASTEC, STFC Daresbury Laboratory, Warrington WA4 4AD, United Kingdom*



(Received 14 October 2019; accepted 23 March 2020; published 16 April 2020)

EuroCirCol is a conceptual design study of a post-LHC, Future Circular Hadron Collider (FCC-hh) with 50 TeV of beam energy and 100 km long, which aims to expand the current energy and luminosity frontiers. The vacuum chamber of the FCC-hh will have to cope with unprecedented levels of synchrotron radiation power for proton colliders, dealing simultaneously with a tighter magnet aperture. Considering that the high radiation power and photon flux will release larger amounts of gas into the system, the difficulty to meet the vacuum specifications increases substantially compared with the LHC. This paper presents a study on the beam induced vacuum effects for the FCC-hh novel conditions, the different phenomena which, owing to the presence of the beam, have an impact on the accelerator's vacuum level. It is concluded that thanks to the adopted mitigation measures the proposed vacuum system shall be adequate, allowing us to reach $\leq 1 \times 10^{15}$ $\text{H}_{2eq}/\text{m}^3$ with baseline beam parameters within the first months of conditioning.

DOI: [10.1103/PhysRevAccelBeams.23.043201](https://doi.org/10.1103/PhysRevAccelBeams.23.043201)

I. FCC-hh VS LHC. NEW CHALLENGES

The Future Circular Hadron Collider (FCC-hh) is a 100 km long particle collider, being developed in the frame of the EuroCirCol conceptual design study. It is designed to be the Large Hadron Collider's (LHC) successor, and it is aimed at expanding the current energy frontiers and the understanding of the Standard Model [1,2].

The FCC-hh involves two superconducting proton storage rings circulating in opposite directions and colliding at the energy of $E = 50$ TeV per beam, a considerable step forward compared to the LHC, designed to reach 7 TeV. To avoid an unaffordable machine length, the maximum dipole magnetic field is raised from 8.3 T up to 16 T. The high proton energy and magnetic field lead to a dramatic increase in the synchrotron radiation (SR) critical energy (ϵ_c), going from 43.8 to 4286 eV [see Eq. (1)]. Even if the maximum beam current is expected to be lower than in the LHC (see Table I) the photon flux is increased due to the much higher magnetic field, as represented by Eq. (2) (derived from the expressions found in [3,4]):

$$\epsilon_c [\text{eV}] = 1.074 \times 10^{-1} E^2 [\text{TeV}] B [\text{T}] \quad (1)$$

$$\dot{\Gamma}_{ph} [\text{ph}/(\text{m s})] = 2.101 \times 10^{13} I [\text{mA}] B [\text{T}]. \quad (2)$$

$\dot{\Gamma}_{ph}$ is defined as the SR photon flux, B the dipole magnetic field and I the proton beam current. The higher $\dot{\Gamma}_{ph}$ and ϵ_c of the FCC-hh are translated in an increase of emitted power per bending magnet (MB) length, going from the 0.22 W/m present in the LHC to 35.4 W/m. In order to optimize the cooling efficiency, the beam screen (BS) temperatures are raised from 5–20 K window up to 40–60 K. All these conditions are unprecedented for a proton collider. Up to date no proton accelerator has been

TABLE I. Comparison of the LHC's and the FCC-hh's relevant baseline parameters [2,5].

	LHC	FCC-hh
Energy [TeV]	7	50
Current [mA]	580	500
Circumference [km]	26.7	97.75
Dipole magnetic field [T]	8.33	15.96
Photon flux [ph/(m s)]	1×10^{17}	1.7×10^{17}
SR power [W/m arc MB trajectory]	0.22	35.45
SR critical energy [eV]	43.8	4286.3
Angle between dipoles [°]	0.29	0.077
Beam screen temperature [K]	5–20	40–60

Published by the American Physical Society under the terms of the Creative Commons Attribution 4.0 International license. Further distribution of this work must maintain attribution to the author(s) and the published article's title, journal citation, and DOI.

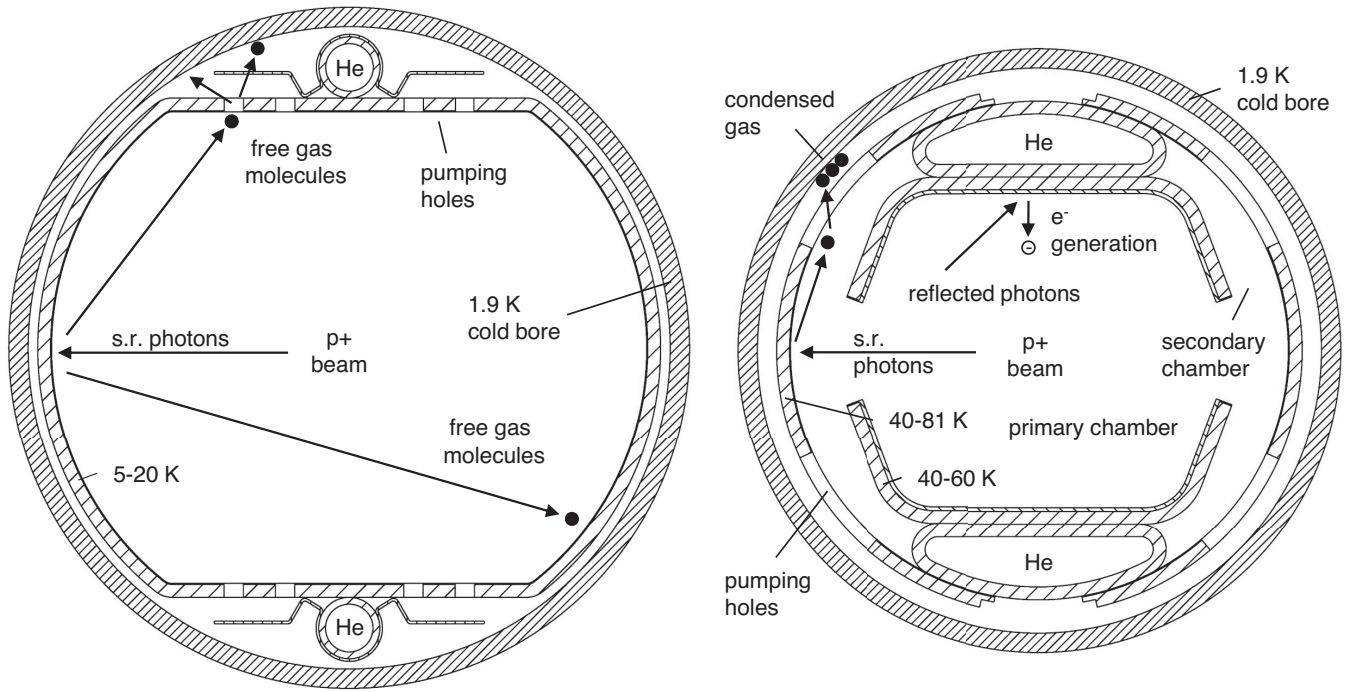


FIG. 1. Comparison of the beam screen of the LHC, as seen in [10], and the FCC-hh's. Both figures are represented at the same scale. The inner diameter of the cold bore is 50 mm in the LHC and 44 mm in the FCC-hh.

built being able to achieve SR power densities in the order of electron light sources.

As it is known, the outgassing related to photon stimulated desorption (PSD) scales with ϵ_c [6]. The density of the electron cloud (e^- cloud), effect responsible of gas release through electron stimulated desorption (ESD), depends on the photoelectron generation, which in turn scales with ϵ_c as well. Considering the ϵ_c increase with respect to previous machines, meeting beam vacuum specifications in the FCC-hh is not expected to be straightforward. Vacuum specifications are defined by the beam-gas interaction rate (R):

$$R = \sum_j \sigma_j n_j = \sigma_{H_2} \sum_j \frac{\sigma_j}{\sigma_{H_2}} n_j \quad (3)$$

where the index j represents each gas species in the vacuum chamber, n the gas density and σ_j the nuclear scattering cross section. This allows to introduce the H_2 equivalent gas density term ($n_{H_{2eq}}$), which represents the addition of all the gas species into one single gas density value:

$$n_{H_{2eq}} = \sum_j \frac{\sigma_j}{\sigma_{H_2}} n_j \quad (4)$$

being $\leq 1 \times 10^{15} H_{2eq}/m^3$ the value of $n_{H_{2eq}}$ which meets the vacuum specifications in the FCC-hh [7].

In this document each phenomena responsible of the gas density increase is separately studied, using the vacuum chamber geometry and the gas load mitigation measures

proposed in a previous publication [7]. Ultimately, the feasibility of the FCC-hh vacuum system is assessed.

II. THE FCC-HH BEAM SCREEN

The BS is the main element of the vacuum chamber. Its principal purpose is to intercept the SR power emitted by the beam and dissipate it at higher temperatures than the magnet cold bore (CB) (40–60 K vs 1.9 K). In this way, the Carnot efficiency is increased, and the total power of the cryoplants stays within reasonable values [8].

Figure 1 displays a comparison of the BS proposed for the FCC-hh and the one present in the LHC. Both beam screens are represented at the same scale. The basic principle of operation is the same in both of them. The SR impacts on a highly absorbing area (the sawtooth surface) to minimize the SR scattering, photoelectron production and the gas load. The released gas is pumped through a series of perforations on the BS which lead to the CB. The CB is cold enough to condense all the H_2 molecules hitting its surface, yielding a sticking probability of ≈ 1 [9]. This is the only means of pumping in the arcs during the machine operation.

The main differences are the cooling channel size, enlarged in the FCC-hh BS to allow a higher cooling capacity, and the double chamber layout. This new layout aims to reduce the transverse coupling impedance of the pumping holes, to avoid the direct impact of SR and electrons on the cold mass and to lower the photon flux arriving to the critical areas where the e^- cloud build up

happens. These critical areas, as explained in [7,11], are intended to be treated with laser ablation surface engineering (LASE) [12–14] or coated with amorphous carbon (a-C) [15,16] in order to mitigate the secondary electron yield (SEY) and thus suppress the e^- cloud. Owing to the easiness of LASE application and the higher potential in SEY and gas load reduction, it is preferred over a-C. Recent studies in the SPS have proved the efficiency of LASE [17]. This new feature will also be beneficial to lower Cu's ESD [18], and if applied on the sawtooth edges, PSD as well [19].

Both of these solutions have a very high specific surface and a high gas adsorption capacity, surpassing even by a factor of 100 that of a flat Cu surface. Although during an ideal operation, a large gas coverage is not expected to be present on the BS, uncontrolled temperature regulations or magnet quenches could cause a gas redistribution and increase its amount. A temperature transient could lead then to undesired gas density peaks, if the desorption window of the chosen SEY solution falls within the temperature variation range [20]. To avoid this, the BS temperature might be adjusted by around ± 20 K, as it happened to the HL-LHC BS [21]. Nonetheless, since the exact specifications of the SEY mitigation solution for the FCC-hh, and thus its desorption window, are not fully defined yet, this remains as future work. The impact of this temperature adjustment on the vacuum performance is expected to be minimal. In a standard dynamic mode, the electron and photon bombardment on the BS surface keep the coverage low, in equilibrium. In static mode, the residual gas density is minimal and not sufficient to grow a significant coverage during turnaround times.

Being the pumping holes of the FCC-hh BS screened from the proton beam, their contribution to the beam impedance budget is negligible. Therefore, they are allowed to be much larger than in the LHC. The only

limitation in their size is the amount of radiation leaked to the cold mass. The increased hole size, altogether with the mentioned augment in the BS temperature, result in a very high pumping speed. In the FCC-hh BS, the H_2 pumping speed is 898 l/(s m) at 40 K, and in the LHC 490 l/(s m) at 40 K [7] (and 173 l/(s m) at 5 K). The higher temperature of the FCC-hh BS has nevertheless some detrimental effects on the collider's performance, since the PSD molecular yield, the heat transmission to the cold mass and the Cu surface resistance scale along with it.

The 1.9 K CB is present in almost all the length of the arcs with the exception of the cryostat interconnections, in which there are around 0.4 m without any H_2 pumping. The low conductance of the BS (derived from its low diameter) added to this lack of pumping, may cause the gas density to increase around one order of magnitude in these regions.

To avoid virtual leaks due to flat-flat contact surfaces, the cooling channel is welded to the inner and outer BS components leaving periodic clearances. The possible molecule reservoirs between the flat surfaces can be thus evacuated. The good vacuum performance of the BS design has been benchmarked at BESTEX [22], a dedicated experimental setup built in the frame of the EuroCirCol project. It has been designed to explore PSD, photon heat loads, photon reflectivity and photoelectron generation originated in the inserted FCC-hh BS prototypes under SR irradiation, with a SR spectrum similar to the FCC-hh's one. At BESTEX, a BS prototype with the latest design has been tested both at RT and 77K, satisfactorily showing the absence of virtual leaks.

III. BEAM INDUCED VACUUM EFFECTS

A. General gas density expression

In equilibrium state, n_j in the vacuum chamber can be expressed as follows, in a simplified way:

$$n_j = \frac{\overbrace{\dot{\Gamma}_{ph}(\eta_{ph,j} + \eta'_{ph,j})}^{\text{photon-stimulated desorption}} + \overbrace{\dot{\Gamma}_e(\eta_{e,j} + \eta'_{e,j})}^{\text{electron-stimulated desorption}} + \overbrace{\sum_k \{(\eta_{i,k,j} + \eta'_{i,k,j})\sigma_{i,k}(I/e)n_j\}}^{\text{ion-stimulated desorption}} + \overbrace{Aq_j}^{\text{thermal outgassing}}}{S_j} \quad (5)$$

where S_j is the BS pumping speed for each gas species, η_{ph} and η'_{ph} are the primary and secondary photon molecular desorption yields (with different values for each species, as the other molecular yield terms), η_e and η'_e the primary and secondary electron molecular desorption yields, $\dot{\Gamma}_e$ the electron impingement rate, η_i and η'_i the primary and secondary ion desorption yields, σ_i the ionization cross section, k represents each ionized gas species impacting against the surface of the chamber, A the surface area of the studied volume and q the thermal outgassing rate. All the mentioned yields depend directly on the energy of the corresponding impinging particle.

Considering that the sticking probability is the same for all gas species, S_j can be found with Eq. (6):

$$S_j = S_{H_2} \sqrt{M_{H_2}/M_j} \quad (6)$$

where M represents the molar mass of the gas (j). Each one of the first three terms of Eq. (5) with an overbrace symbolizes the gas load of one beam induced vacuum effect. During beam runs at nominal conditions, PSD is expected to feature the highest outgassing rate as long as ESD is effectively suppressed. The contribution of the

thermal outgassing to the total gas load in dynamic mode is considered negligible, owing to the low temperature of the system. However, it is the only outgassing source during static mode along with the vapor pressure of the condensed gases in the vacuum chamber. These two effects alone are expected to result in a static n_j around two orders of magnitude lower than the dynamic one.

The four most common gas species of a cryogenic vacuum system have been taken into account in this study, i.e., H_2 , CO , CO_2 and CH_4 . The gas load and, ultimately, the partial gas density (n_j) of each beam induced vacuum effect have been calculated, applying the formula shown above separately for each different gas species. Afterwards, they have been added together in H_2 equivalent units to obtain the total gas density value. The global gas composition and the contribution ratios of each effect respect to the total gas density are also calculated and presented in Sec. IV.

B. Primary photon stimulated desorption (PSD)

Knowing the $\dot{\Gamma}_{ph}$ map along the vacuum chamber (in area units), and knowing the η_{ph} of the irradiated material, the gas load of this effect can be easily calculated for any required photon dose. The $\dot{\Gamma}_{ph}$ map has been calculated using SYNRAD+ [23] in units of photons per cm^2 , as explained in [7]. SYNRAD+ supports the exportation of the obtained data to MOLFLOW+ [24–26], allowing a direct calculation of the resulting gas density in the modeled vacuum chamber adding $\eta_{ph,j}$ as an input. For the η_{ph} of Cu and P506 stainless steel [27] (the BS's materials) at the mentioned conditions, 40–60 K and for a SR with ϵ_c of 4.3 keV, there is neither exact nor similar experimental data in the literature. It is expected to be experimentally measured in the future with BESTEX. Lacking for the time being the necessary data, they have been numerically estimated, starting from the closest published values and then scaling them according to the variation in critical energy and/or temperature. For Cu, data from the LHC PSD tests has been chosen [28], taken at 77 K and with a SR ϵ_c of 50 eV. For P506 SS, lacking suitable cryogenic experiments, data at 3.75 keV ϵ_c and RT [29] has been chosen because of the lack of bake-out and because of the closeness of its ϵ_c to the FCC-hh's one (4.3 keV). The complete process used to convert these chosen yields to the theoretical ones with the FCC-hh conditions is hereunder detailed.

For the most common materials used in vacuum technology, η_{ph} is in the range of 10^{-3} – 10^{-5} molecules/photon, with H_2 generally featuring the highest yield. η_{ph} decreases over the photon dose that the surface receives. It is usually plotted separately for each species on a log-log scale, starting with a constant, high yield, until a cutoff value of about 10^{19} – 10^{20} ph/m, corresponding to the time when the cleaning of the surface starts (see Fig. 4).

After this initial plateau, the curve follows the following empirical expression [Eq. (7)] [25,30]. No change of slope is usually appreciated for doses up to 1×10^{23} ph/m.

$$\eta_{ph}(D) = \eta_0 D^a \quad (7)$$

η_0 is defined as the initial yield, D is the integrated photon dose, usually expressed in ph/m in the literature, and a is the decaying slope (in log-log scale), with values usually ranged between -0.6 and -1 .

The standard units of photon dose, in ph/m, even if they are useful for fast calculations, are nonetheless not valid as an input for MOLFLOW+. They also have little physical meaning, since PSD is a surface effect and has to be expressed in terms of flux/area instead of flux/length. Two experiments with the same irradiation in terms of chamber length, and same flux, could have a different SR beam width and could be cleaning a different amount of the vacuum chamber, besides of the scattering effect which can distribute the radiation all over the chamber and not only on the initially irradiated areas. As such, the available dose data has been firstly converted from ph/m to ph/cm^2 .

The conversion methodology was initially proposed in [25], where an original experiment built to acquire PSD data was recreated in SYNRAD+ to know the proportion of irradiated chamber area per chamber length. A similar process has been followed in the presented study for the Cu and P506 SS initial data. The original experiments were simulated, and the area of irradiation measured. SR specular scattering has also been taken into account, filtering the areas receiving small amount of SR power. For SS data, it has been found that around 70 ph/m linear dose of the published data correspond to $1 ph/cm^2$ of surface dose, similarly to [25]. For Cu, it has been decided to take the same factor as a pessimistic estimation, even if this factor has been found to be much larger due to a higher SR beam height of the original experiment, and consequently a larger irradiated chamber area. That said, it is relevant to highlight the fact that for high photon doses, the error in the estimations is reduced to a minimum, given the general convergence of η_{ph} in common technical materials.

Next, the base yield of the selected data has been increased taking into account the greater ϵ_c of the FCC-hh SR. η_{ph} increases along with ϵ_c because, on one hand, a larger percentage of the SR spectrum is emitted with an energy higher than the work function of the material (≈ 4 eV for Cu), being able to trigger photoelectron emission in the surface, a phenomenon which is thought to mediate PSD. On the other one, and for the studied energy range, higher photon energies mean higher photoelectron energies, more chances to interact with the present molecules and a higher number of secondary electrons which in turn can desorb larger amounts of gas. The LHC's and FCC-hh's SR spectrums are plotted in Fig. 2, where it

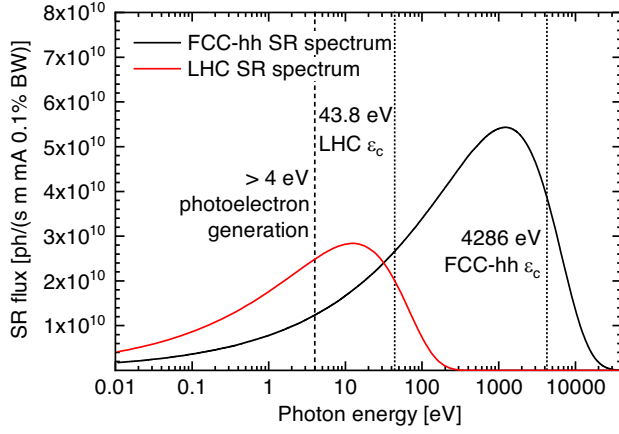


FIG. 2. Comparison of the FCC-hh SR spectrum vs the LHC's, highlighting the critical energy values. Figure taken from [7].

can be seen the much higher proportion of photons above 4 eV.

The dependence of η_{ph} on ϵ_c was found in the past to fit the following empirical expression [6]:

$$\eta_{ph} = C\epsilon_c^b \quad (8)$$

where C and b are positive constants different for each gas and material. b values are usually located between 0.7 and 1.2.

Figure 3 shows an example of the dependence of η_{ph} on ϵ_c , using experimental data from the literature [6,31] for baked Cu at room temperature (RT). The shown dependence has been used to raise the original data up to the energy relevant for the FCC-hh.

Even if using data taken at RT, the analysis keeps its pessimistic approach as the variation at high temperatures is expected to be higher than in cryogenic conditions. Besides, the extrapolated data corresponds to surfaces irradiated with glancing incidence, yielding outgassing rates much higher than with a perpendicular one (as it

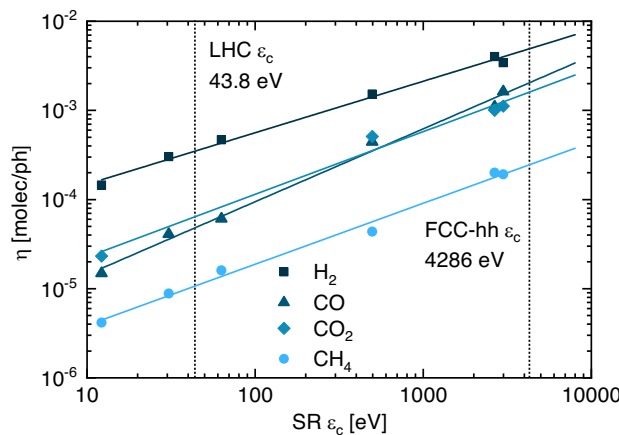


FIG. 3. η_{ph} dependence on ϵ_c for RT baked Cu, read at a common dose of 2.5×10^{20} ph/m, using data from [6,31].

happens for the Y_{ph}), which is the case of the FCC-hh, thanks to the sawtooth finishing. The real η_{ph} is expected to be lower, then, as it was recently seen in BESTEX [19,32].

For P506 SS, since starting data at RT has been chosen, the dependence of the η_{ph} with the temperature published in [33] for a fixed dose has been used to estimate the required data for the FCC-hh conditions. Nevertheless, P506 SS has very little impact on the total gas load, since Cu is the material of the BS which receives most part of the SR.

The obtained η_{ph} for each gas were exported to MOFLOW + along with the calculated $\dot{\Gamma}_{ph}$ map [7] to obtain the partial gas densities of each species.

By combining Eqs. (4)–(6) one can rewrite Eq. (5) for primary PSD in a more compact form:

$$n_{H_{2eq}} = \frac{\dot{\Gamma}_{ph}}{S_{H_2}} \eta_{ph,H_{2eq}} \quad (9)$$

where

$$\eta_{ph,H_{2eq}} = \eta_{ph,H_2} \sum_j \left(\frac{\eta_{ph,j} \sigma_j}{\eta_{ph,H_2} \sigma_{H_2}} \sqrt{\frac{M_j}{M_{H_2}}} \right) \quad (10)$$

and, simplifying:

$$\eta_{ph,H_{2eq}} = \eta_{ph,H_2} K_{\eta_{ph}} \quad (11)$$

The estimated η_{ph} values have been converted to the above shown H_{2eq} units ($\eta_{ph,H_{2eq}}$) to allow a direct assessment of the quality of each material with regard to their impact on the vacuum level. $\eta_{ph,j}$ have been added together according to their equivalence to H_2 in terms of the amount of beam-gas interaction that each different species represents. $\eta_{ph,H_{2eq}}$ can also be understood as a conversion of all different molecules into H_2 ones (see Table II), which allows to approximately obtain the same value of $n_{H_{2eq}}$ as if we separately added together all the partial n_j following Eq. (4).

The coefficient $K_{\eta_{ph}}$ varies with the choice of material, its treatments, photon dose, etc. For example, it varies with photon dose: from 8 to 5 for Cu irradiated with $\epsilon_c = 50$ eV at 77 K [28], from 50 to 30 for baked Cu irradiated with $\epsilon_c = 3.75$ keV at RT [35], and from 50 to 20 for non-baked SS irradiated with $\epsilon_c = 3.75$ keV at RT [29]

TABLE II. Equivalences to H_2 of the different gas species.

Gas species (j)	σ_j/σ_{H_2} [34]	S_{H_2}/S_j	Total H_{2eq}
H_2	1	1	1
CH_4	6.0	2.8	16.8
CO	9.0	3.7	33.5
CO_2	13.9	4.7	64.9

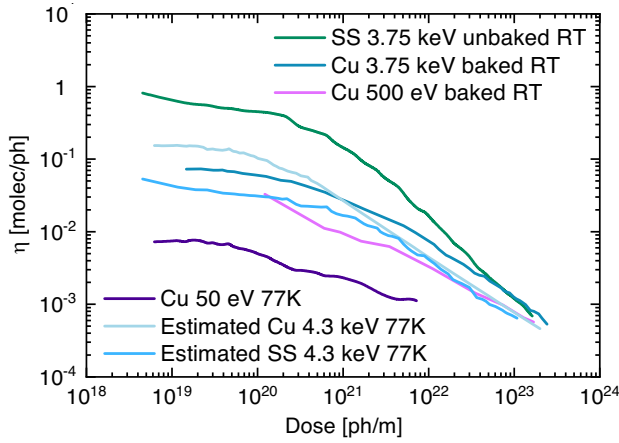


FIG. 4. H_2 equivalent molecular PSD yields ($\eta_{ph,H_2,eq}$) for various common materials and conditions [28,29,35,36] compared with the estimated yields for the FCC-hh.

(approximated values). This shows that the weight of H_2 in the total beam-gas interaction ratio can be insignificant compared to the other gas species such as CO_2 and CO .

The found $\eta_{ph,H_2,eq}$ values of the BS materials are plotted in Fig. 4 and compared with other $\eta_{ph,H_2,eq}$ in the literature.

The resulting curves are quite similar for both Cu and steel, being placed between the data taken at RT with high ϵ_c and at 77 K with low ϵ_c , as expected. Even if the η_{ph} of H_2 does not decrease much when lowering the temperature, (by a factor of two, for 45.3 eV ϵ_c and normal incidence [33]), the CO_2 's η_{ph} can be decreased by a factor of 30. Being each desorbed CO_2 molecule equivalent to ≈ 65 molecules of H_2 (see Table II) the total H_2 equivalent yield is dramatically reduced.

It can also be noticed how most of the RT curves end up converging on the same yield after reaching a dose of 1×10^{23} ph/m, when the surface is considered already conditioned. This effect is thought to be ascribed to the gas content depletion, the hybridization of the sp^3 surface carbon layer into sp^2 carbon [37] and the increase of the carbon concentration in the irradiated areas [38]. The growth of the sp^2 carbon layer is translated into similar Y_{ph} ultimate values in the different original surfaces.

C. Secondary photon stimulated desorption (PSD', gas recycling)

It is known that the total PSD molecular yield increases along with the gas coverage on the irradiated surfaces. The gas molecules accumulated on a cold surface are released back into the system when high energy photons impact onto it, presenting molecular yield values much higher than those of a clean surface. This so-called recycling effect is represented by the secondary molecular yield (η'_{ph}), which must be taken into account during the design of a cryogenic vacuum system. Besides of the interception of the heat load at higher temperatures, the recycling effect is another

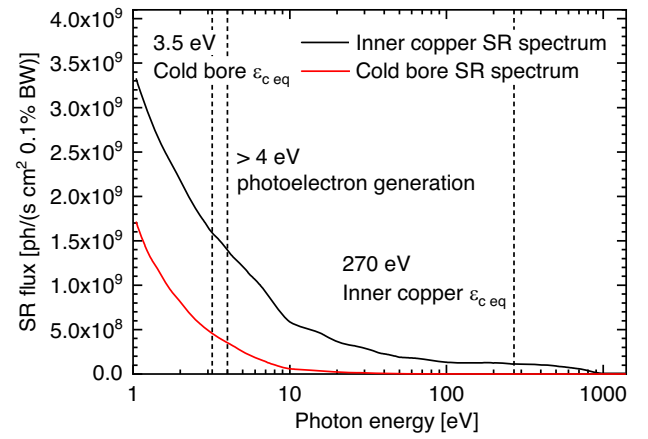


FIG. 5. Spectrum of the SR arriving to the CB and to the inner chamber [7], with most part of their photon flux below Cu's work function. Calculated with SYNRAD+. Figure taken from [7].

reason of using a beam screen, since the continuous photon and electron impact on the 1.9 K pumping surfaces would remove the gas being condensed, not allowing the coverage to grow and rising the gas density in the system over time until eventually surpassing the established limit.

In this study only the η'_{ph} of the 1.9 K area, the CB (see Fig. 1), has been taken into account. The BS inner surface coverage has been considered to be in equilibrium, with a coverage under the monolayer, balanced by the constant removal of adsorbed gas by the scattered SR, ions and impinging electrons and by the sticking coefficient the surface presents at the defined range of temperatures [39].

In the proposed design, the cold mass never gets directly irradiated by the SR. However, around 1% of the total emitted photon flux above 1 eV succeeds in reaching the CB through the pumping holes after hitting the sawtooth surface. Fortunately, the equivalent critical energy ($\epsilon_{c,eq}$) of the photon flux reaching the cold mass is extraordinarily low, less than 3.5 eV, given that high energy photons have a very low probability of being reflected after hitting a perpendicular surface. Fig. 5 shows the calculated energy spectrum of the SR arriving to the CB and inner chamber, cropped at 1 eV, where it is possible to see the low energy of the radiation arriving to the bore, in the range of visible and UV mostly. As for the SR power, much less than 0.01% of the total emitted one is expected to be leaked up to the CB.

To calculate the gas load of this effect, the evolution of the surface coverage has been estimated for a period of two years, the established time in the LHC between allowed cold mass warm-ups. As a conservative estimation, it has been considered that all the gas desorbed inside the BS due to PSD and ESD is uniformly accumulated on the area next to the pumping holes, about 10 mm wide, with a perfect sticking factor of 1. In reality, the gas desorbed from the CB could be distributed over all its surface. Calculated values are shown in Fig. 6.

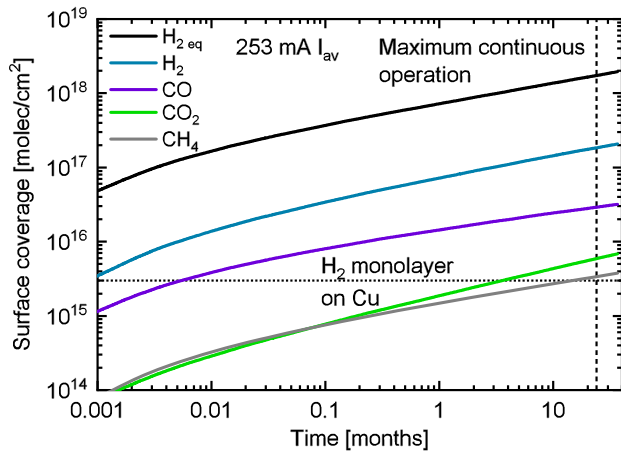


FIG. 6. Worst case of estimated surface coverages on the CB over time, for a continuous operation during Phase I [40].

To each coverage value a η'_{ph} has been assigned using experimental data from the literature [41]. These values are shown in Table III for a particular time frame. H_2 is the gas most easily desorbed, presenting a very high η'_{ph} , almost 3 orders of magnitude higher than η_{ph} . For this gas, it does not vary in excess after the monolayer ($\approx 3 \times 10^{15}$ molecules/cm² [42]). The rest of the species have a much more varying secondary yield value within the range of the primary one. It is not expected to surpass 10^{-4} molecules/photon over the two years of operation. Therefore, the composition of the recycled gas would be mainly H_2 in more than 90%.

With the displayed yields and the $\dot{\Gamma}_{ph}$ map found in [7], the recycling gas load can be easily calculated, as shown in Eq. (5). It is concluded that, thanks to the sawtooth finishing and the pumping holes layout, the SR power reaching the cold bore is kept within safe values, and does not entail an unaffordable desorption of the condensed gas.

It is also relevant to highlight that the experiment from which the chosen η'_{ph} values are taken was performed with a ε_c of 284 eV, far greater than the $\varepsilon_{c,eq}$ of the photons arriving to the CB. These data have been chosen since no data for a lower ε_c is available. The published values have been used without any conversion as a pessimistic

TABLE III. η'_{ph} over time, in molecules/photon, as interpolated from the experimental data published in [41] and calculated for the coverage values shown in Fig. 6.

Gas species (g)	1 week	1 month	1 year	2 years
$H_{2,eq}$	0.53	0.54	0.60	0.61
H_2	0.51	0.51	0.55	0.56
CO	3.3×10^{-4}	3.7×10^{-4}	5.2×10^{-4}	5.9×10^{-4}
CO ₂	1.3×10^{-4}	1.6×10^{-4}	3.2×10^{-4}	4.2×10^{-4}
CH ₄	3.4×10^{-4}	3.8×10^{-4}	5.3×10^{-4}	6.2×10^{-4}

estimation, yielding even so gas load values relatively low. Future experiments at 1.9 K would be necessary to properly assess the stability of the condensed gas.

As for the photocracking effect [43,44], process where the adsorbed CO₂ and CH₄ dissociate into CO + O₂ and C + H₂ due to the interaction with the incident radiation, it has not been considered for the calculations. Most of the photons arriving to the CB have an energy lower than the necessary one to break the chemical bonds, so it is not expected to influence the gas composition in a high extent. Moreover, part of the C present in the cracked molecules is not expected to be released as a gas, lowering the total H₂ equivalence of the released species. Consequently not taking this process into account results in a conservative scenario.

Another effect which is expected to take place is the gas recycling by means of the thermal radiation coming from the BS. This phenomena was reported to prevent the saturated vapor pressure to go below of only 10^{-10} – 10^{-11} mbar, without observed dependence on the BS temperature within 20–100 K, and it was attributed to the surfaces at room temperature [45]. Therefore, even with the difference of BS temperature, it is not expected to have a significant impact on the beam lifetime.

D. Electron stimulated desorption (ESD)

As previously explained, the e^- cloud effect is expected to be suppressed in the FCC-hh thanks to the application of LASE (the preferred and hereby studied option) and/or a-C on the beam screen.

Even if the electron impingement rate ($\dot{\Gamma}_e$) on the vacuum chamber would be considerably low, mainly thanks to the SEY mitigation, it can still trigger some non-negligible gas desorption through ESD. The ESD contribution to the total n_j must be then taken into account.

The ESD gas load can be calculated multiplying η_e by $\dot{\Gamma}_e$ [see Eq. (5)]. An estimation of η_e for Cu at cryogenic temperature and with electron energy of 300 eV can be found in [46]. Lacking data for LASE, these values have been conservatively chosen as a pessimistic scenario. η_e depends on the incident electron energy [47] following the same empirical expression as for η_{ph} [Eq. (8)]. For each material, η_e is usually proportional to η_{ph} and Y_{ph} . LASE's η_{ph} has been found to be much lower than untreated Cu during the latest runs in BESTEX [19], as well as its Y_{ph} [48–50], as described in [7]. Consequently, even if still not measured, LASE's η_e values are expected to be lower than Cu's, being safe to use the values found in [46].

$\dot{\Gamma}_e$ has been calculated with the PYECLOUD code [51,52] for 1–1.8 SEY and different bunch spacing options, and for 50 TeV, 500 mA beam. $\dot{\Gamma}_e$ depends directly on the photoelectron generation rate, N_e , which is directly calculated with $\dot{\Gamma}_{ph}$ and Y_{ph} , using Eq. (12):

TABLE IV. Worst case of $\dot{\Gamma}_{ph}$ (calculated using pessimistic sawtooth reflectivity properties) above 4 eV and subsequent N_e on different BS regions. 50 TeV, 500 mA beam. Inner chamber e^- cloud build-up areas and photon absorber are considered to be treated with LASE. Rest of the showed regions are OFE Cu.

Beam screen area	$\dot{\Gamma}_{ph}$ [ph/(cm ² s)]	N_e [e ⁻ /(cm ² s)]
SR absorber central region	4.0×10^{16}	5.9×10^{15}
Sawtooth stopping facets	1.8×10^{16}	2.4×10^{15}
SR beam tails screen	1.6×10^{13}	8.7×10^{11}
Interconn non-SR areas	1.2×10^{13}	5.0×10^{11}
Quad e ⁻ impact regions	9.4×10^{12}	1.6×10^{11}
Dip e ⁻ impact regions	1.9×10^{12}	2.3×10^{10}

$$N_e = \int_{E_{\min}}^{E_{\max}} \dot{\Gamma}_{ph}(E) Y_{ph}(E) dE \quad (12)$$

N_e results for some representative BS areas are shown in Table IV.

The most critical areas to analyze are the regions close to the beam which delimit the magnetic field lines [53]. They can be appreciated in Fig. 7, for quadrupoles and dipoles. N_e on these areas has got the highest weight in $\dot{\Gamma}_e$ final values, so they should be the ones protected the most from SR incidence and/or treated for SEY mitigation.

$\dot{\Gamma}_e$ values are shown in Figs. 8, 9, and 10, for dipoles, quadrupoles, and drift spaces between dipoles. $\dot{\Gamma}_e$ is projected on the horizontal direction in the BS for a bunch spacing of 25 ns, the design value. The abscissa axis represents the horizontal width of the BS, whose inner radius, measured in the secondary chamber, is 19.425 mm. The point $x = 0$ mm represents the vertical plane where the proton beam is positioned.

These data have been used in Eq. (5) to calculate the ESD gas load for 25 ns, which is shown in Sec. IV. For dipoles and quadrupoles, an SEY = 1 and Y_{ph} LASE values [50] are considered. For the drifts between dipoles, the SEY has been set to 1.4 and Y_{ph} Cu data [50] have been used. No magnetic field has been taken into account in these regions as a pessimistic scenario, even if the magnetic

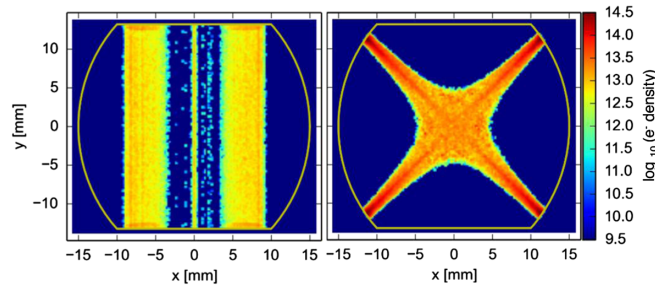


FIG. 7. Electron density graphs for an LHC-type BS and SEY curves Cu-like, for baseline parameters. On the left, BS in a dipole magnetic field, on the right in a quadrupole magnetic field. Figure taken from [7].

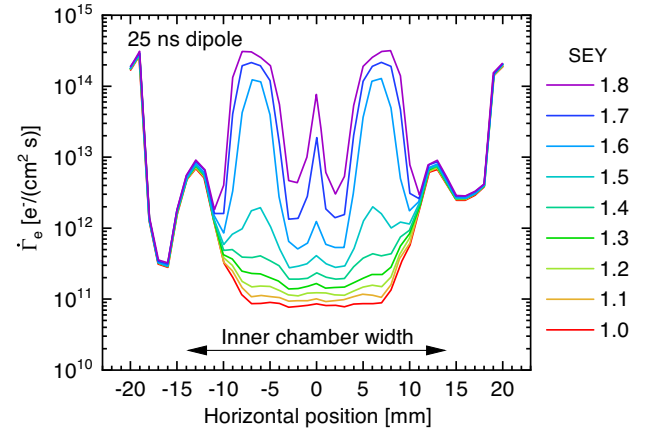


FIG. 8. Horizontal projection of the electron impingement rate inside the FCC-hh BS with a 16 T dipole magnetic field, depending on the SEY. 50 TeV, 500 mA, 25 ns beam. Inner chamber flat areas treated with LASE.

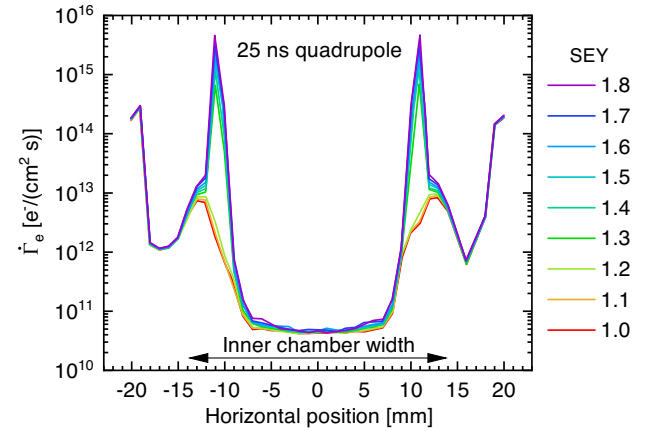


FIG. 9. Horizontal projection of the electron impingement rate inside the FCC-hh BS with a 360 T/m quadrupole magnetic field, depending on the SEY. 50 TeV, 500 mA, 25 ns beam. Inner chamber curved areas with LASE.

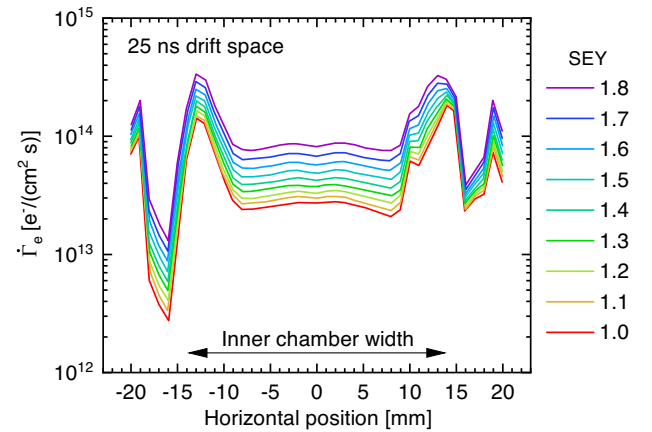


FIG. 10. Horizontal projection of the electron impingement rate inside the FCC-hh BS in the interconnect area, with no magnetic field, depending on the SEY. 50 TeV, 500 mA, 25 ns beam. Only absorber slope region treated with LASE.

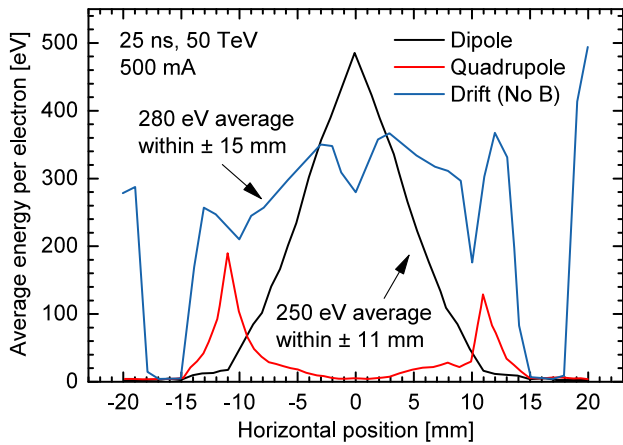


FIG. 11. Average electron impact energy in a dipole and drift space with $SEY = 1.4$, and in a quadrupole with $SEY = 1.1$. 50 TeV, 500 mA, 25 ns beam. Drift space without magnetic field presence.

field in the magnets interconnects is far from being negligible.

$\dot{\Gamma}_e$ has been generally found to be very low in dipoles and quadrupoles with $SEY \leq 1.0$, the maximum value of the proposed LASE option for the FCC-hh BS [54], for 0–1000 eV electron energies. In the drifts, however, $\dot{\Gamma}_e$ is considerably high owing to the presence of the photon absorber, with a high SR power density, and owing to the absence of an SEY mitigation treatment in the other elements. In total, provided the SEY is set under the multipacting threshold [2,7], it produces a considerably small rise in the gas density for all the possible bunch spacing options (25 ns, 12.5 ns, 5 ns), representing in average 10% of the total gas density in the arcs for the 25 ns bunch spacing option.

In order to avoid electron multipacting, leaving the vacuum chamber without SEY mitigation treatment is only possible in dipoles and drifts, for 25 ns and 5 ns [7]. In dipoles, for a scrubbed Cu with a defined $SEY = 1.4$, the ESD gas load has been estimated to be two times higher than for LASE treated Cu. This option would entail a further conditioning of the BS until being able to reach the baseline current and energy parameters with a nuclear scattering beam lifetime above 100 h, adding approximately 20 Ah of necessary dose.

The average electron impact energies have also been calculated. An example for the 25 ns baseline is displayed in Fig. 11, plotting the values as an horizontal projection. In all the three studied magnetic field variations the electron energy remains always under 300 eV, making the chosen η_e data [46], with 300 eV electron energy, an even further conservative choice.

In this figure it is also possible to appreciate the low energy of the electrons in the secondary chamber of the BS in the dipoles and quadrupoles, starting at around ± 14 mm

in the horizontal length. The electrons generated in the sawtooth surface, where most part of the SR impacts, are far from the positive space-charge potential generated by the beam, and since they are forced to follow the magnetic field lines, they receive a very small kick when a bunch passes.

As for the photoelectrons generated well inside of the secondary chamber, behind the inner chamber, the amount of energy increase is negligible. The inner chamber shields completely the electric field generated by the bunches, preventing the generated photoelectrons from being accelerated. This feature is especially relevant because the CB would otherwise receive a significant heat load from the electrons leaked though the pumping holes, and very high amounts of condensed gas in the 1.9 K surface would be desorbed. The electron shield present in the LHC [55] is thus expected to be unnecessary in the FCC-hh.

In the drifts, the 1.9 K cold bore is not present. Therefore, the power which is leaked in this region through the pumping holes is not as dangerous as it would be inside the magnets. Additionally, the simulations with PYECLOUD have been performed considering a BS profile without pumping holes, with an effective N_e on their otherwise empty volume. The shown $\dot{\Gamma}_e$ can be thus considered overestimated.

Thanks to the low electron power leaked though the pumping holes, the recycling effect ascribed to ESD has not been taken into account in the total gas density calculation, neglecting the value of η'_e in Eq. (5).

E. Ion stimulated desorption (ISD)

In proton colliders the beam current that can be stored is limited among other things by the ISD. The positively charged proton beam ionizes residual gas molecules in its path and repels them by the positive space-charge potential. Ions are then accelerated toward the vacuum chamber walls and release some of the stored gas. Since the resulting increase in the gas density exacerbates the ionization rate, an avalanche process may then occur, triggering a gas density overrun when the beam current is high enough [30]. This beam current value is defined as the critical current (I_c).

To calculate the critical current, a simple approach found in [56] for a two gases system has been followed. Two representative areas of the arcs cell have been studied: the BS inside the MBs and short straight sections (SSS); where a constant and distributed pumping speed is present thanks to the cold mass presence, and the magnets interconnects; where no active pumping is present and the pipe conductance plays a major role. As the critical current depends on the capacity of the studied area to evacuate the generated gas, the interconnects will be consequently the system's bottleneck.

With regard to the gas mixtures studied, the combination of CO and CO₂ has been found to be the worst one due to

the high cross section and yields of these species. Values for a mixture of H₂ and CO, the most common species, are shown for comparison.

$$I_c(j, k) = \frac{C_j e}{\eta_{i,k,j} \sigma_{i,k}} \quad (13)$$

Equation (13) represents the partial critical current for a region with a constant distributed pumping (C_j). Complete formulas used for both representative areas can be found in [56]. $\eta_{i,k,j}$ depends on the ion impact energy. Procedures for calculating the energy of ions for round and flat beams are described in [57,58] and [59], respectively. The probability of ionization $\rho(r)$ of the residual gas molecules is proportional to the density of protons in the bunch at the molecule position (r) at the ionization time. For a Gaussian distribution of particles in a round beam:

$$\rho(r) \propto e^{-r^2/\sigma^2} \quad (14)$$

where σ in Eqs. (14) and (15) is the transverse RMS beam size and $r = \sqrt{x^2 + y^2}$ is the radial position. The energy of ions hitting the beam vacuum chamber wall depends on the beam parameters and the initial ion position. The radial electric field, E_b , of the bunch in the FCC-hh can be calculated with Eq. (15):

$$E_b(r) = \frac{q_b}{4\pi\epsilon_0 l_b r} (1 - e^{-r^2/\sigma^2}) \quad (15)$$

where q_b is the proton bunch charge (with a bunch population of 10^{11}), ϵ_0 is the vacuum permittivity and l_b is the RMS bunch length, 8 cm [2]. This expression, for a round beam case, has been chosen for the sake of simplicity. For the case of a more accurate elliptical beam, see [60]. In the model for the calculation of the ion energy, an ionised particle is accelerated by the peak electric field during the bunch passage and then drifts with a constant velocity until the next bunch arrives. A numerical integration method is employed to estimate the ion velocity just before collision with a vacuum chamber wall in the absence of magnetic field. The iteration formulas for the ion velocity v and the radial position r in the presence of a bunch are

$$v_n = v_{n-1} + E_b \frac{q}{m} \Delta t \quad (16)$$

$$r_n = r_{n-1} + v_n \Delta t \quad (17)$$

where $\Delta t = \tau/N$ is the time interval, $n = 1, 2, \dots, N$, and τ is defined as the bunch duration, 0.26 ns. The time interval should be chosen small enough so as not to influence the final result. This requirement was found to be satisfied for $N = 1000$. Between two bunches the ion drifts with velocity $v_d = v_N$ to the radial position r_d when a new bunch arrives:

TABLE V. Average ion energies for different beam sizes, without magnetic field presence. β is the beta function.

Ion species	Arcs ($\beta_{x,y} = 225$ m)	IP ($\beta_{x,y} = 1.1$ m)
H ₂ ⁺	185 eV	16 keV
CO ⁺	142 eV	5.2 keV
CO ₂ ⁺	141 eV	3.7 keV

$$r_d = r_N + v_N(T - \tau) \quad (18)$$

where T is the bunch spacing in seconds. The results of the calculation are shown in Table V, showing the results for the interaction points as well, for comparison. For each set of beam parameters, the ion energy was calculated for different initial positions of the ion across and along the beam, according to the distribution of protons within the bunch. The calculations were performed for H₂⁺, CO⁺, and CO₂⁺. No difference was found between them.

Average ion impact energies with no magnetic field result in around 185 eV for H₂ and 142 eV for CO and CO₂. In the presence of a dipole magnetic field, an energy increase by a factor of 1.05–1.15 was estimated for the LHC for H₂, without any change for CO [58]. For quadrupoles, a factor of 1.3–1.7 was found only for H₂.

$\eta_{i,k,j}$ values estimated for the LHC studies [56] have been chosen as an input for the calculations, with 500 eV for H₂ and 300 eV for the other species. This approach should be safe enough as the real values for the most dangerous species (CO and CO₂) are expected to be lower due to the lower ion energies. The recycling effect has not been considered, as ions are not expected to reach the 1.9 K CB.

As for the cross section values, the estimations for the FCC-hh are displayed in Table VI. They are compared with the ones for previous colliders. They are around a 15% higher than the values found for the LHC due to the higher beam energy.

TABLE VI. Comparison of the ionization cross sections for the FCC-hh and previous proton accelerators, with a clear dependence on the beam energy [61].

Gas species	Beam ionization cross section (σ_i) 10^{-22} m ²		
	SPS 0.45 TeV	LHC 7 TeV	FCC-hh 50 TeV
H ₂	0.36	0.45	0.51
CO	2.2	2.7	3.3
CO ₂	3.4	4.3	5.1
CH ₄	2.5	3.2	3.7

TABLE VII. Results of I_c and related gas density increment in the BS of the arc magnets.

Arc BS inside magnets	H ₂ + CO	CO + CO ₂
I_c	37 A	19 A
Related $\Delta n_{H_2,eq}$	1.4%	2.7%

TABLE VIII. Results of I_c and related gas density increment for the critical area of the MB-MB FCC-hh interconnection.

MB-MB interconnect	H ₂ + CO	CO + CO ₂
I_c	12.8 A	6.8 A
Related $\Delta n_{H_2,eq}$	4.1%	7.9%

TABLE IX. Maximum length of the interconnect for different gas species, at 40 K.

Gas	H ₂	CO	CO ₂	CH ₄
Max length	18.6 m	2.0 m	2.2 m	9.0 m
Safety factor 3	6.2 m	0.68 m	0.73 m	3.0 m

The calculated I_c values are displayed in Tables VII and VIII. Due to the uncertainties of the input parameters in the calculation of I_c , a safety factor of 3 is applied in this work (as recommended in the LHC design studies [56]). The current in the FCC-hh arcs would be limited then to 6.8 A, around 2.2 A taking into account the safety factor. Since the FCC-hh is designed for a baseline beam current of 0.5 A, it is concluded that ISD should not trigger any vacuum instability. However, a slight rise in the gas density is expected owing to the generated ions. It can be easily calculated using Eq. (19).

$$\Delta n_{H_2,eq}(\%) = \frac{100 \times I}{I_c - I} \quad (19)$$

In the worst case, for a gas mixture composed entirely of CO and CO₂, $n_{H_2,eq}$ would rise 7.9% in the middle of the interconnects and a 2.7% inside the magnets. In a more realistic one (see expected composition in Table XI) only 4.1% in the middle of the interconnects and 1.4% inside the

magnets are expected, becoming ISD the beam induced vacuum effect with the smallest contribution to the total gas load in the FCC-hh.

Derived from the same results, it is possible to calculate the critical length of the interconnect region, length at which the pumping speed at its middle point is so low that the beam current reaches its critical value. Equations (20) and (21) have been used to estimate these values for different single gas compositions, shown in Table IX.

$$L_{\max}(j) \approx \pi \sqrt{\frac{u_j e}{\eta_{i,j} I \sigma_{i,j}}} \quad (20)$$

$$u_j \approx \frac{d^3}{3} \sqrt{\frac{\pi R T}{2 M_j}} \quad (21)$$

where u is the specific conductance of the interconnect pipe, d the equivalent pipe diameter and R the ideal gas constant. Results show a maximum pipe length of 0.68 m, taking into account a safety factor of 3 and without considering any sticking coefficients in this region, for any gas. Being 0.4 m the proposed interconnect length without CB, the design shall be safe.

It is also worth mentioning the importance of keeping a low gas coverage in the interconnect, specially during the pumping/cooling down process. η_i values grow considerably fast along with the coverage, being I_c lowered in the same proportion.

IV. MOLECULAR DENSITY PROFILE AND EVOLUTION IN THE ARCS

All the partial gas densities of each gas species, for all the beam induced effects [see Eq. (5)], have been converted to

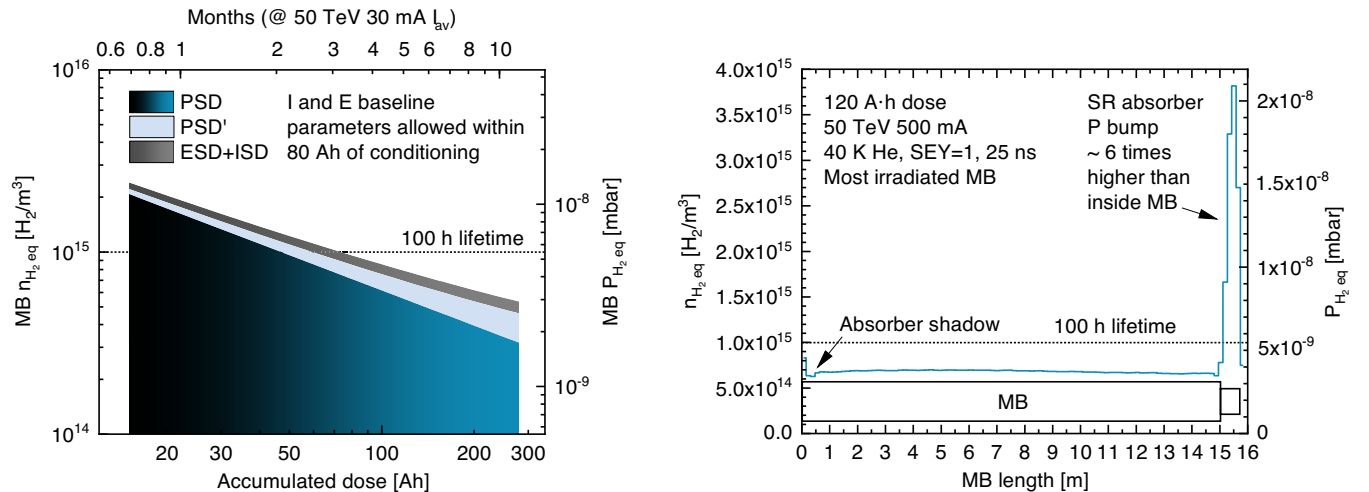


FIG. 12. On the left, $n_{H_2,eq}$ is plotted in H_2,eq units over the accumulated photon dose and its equivalent time in months for 30 mA of average current. On the right, the $n_{H_2,eq}$ profile of the most irradiated MB in the arc cell, representing the periodic profile in the arcs. It is characterized for the bump in the interconnection area, with no cryopumping present for most gas species. Values given for 50 TeV, 500 mA, LASE with an SEY = 1.0 and Cu with a SEY = 1.4, for both subfigures.

TABLE X. Gas load ratios of the beam vacuum induced effects for two different arbitrary doses.

Dose	PSD	PSD'	ESD	ISD
36 Ah	80%	10%	8%	<3%
120 Ah	70%	18%	11%	<3%

$H_{2,eq}$ units [see Eq. (4)] and added together over a series of arbitrary photon doses. They are plotted in the left side of Fig. 12, representing the evolution of the total $n_{H_{2,eq}}$ over time, for a 40 K He MB BS and a 500 mA, 50 TeV, 25 ns beam, with $SEY = 1$. It has been calculated as a pessimistic estimation taking the average $n_{H_{2,eq}}$ along the most irradiated MBs of the arcs cell (the four ones before each short straight section, SSS), which are expected to be the most critical elements in terms of vacuum quality.

According to the obtained results, the goal of 100 h nuclear scattering lifetime, corresponding the previously mentioned gas density of $1 \times 10^{15} H_{2,eq}/m^3$, would be achieved within a dose of 80 Ah, for baseline parameters. It is equivalent to around 4 months of continuous operation with an average current of 30 mA, value similar to that of the first years of the LHC commissioning, with around 300 Ah per year. Running at 50 TeV is still possible before reaching this level of conditioning, but with beam current limitations. Ultimate beam parameters are usually reached only after some years of conditioning, so vacuum is not expected to be a bottleneck in the FCC-hh commissioning out of the initial pump downs.

As expected most of the gas load is caused by PSD, with the other effects playing a minor role. ESD and ISD would be efficiently suppressed thanks to the SEY mitigation treatment and to the high pumping speed of the BS, respectively. PSD' may represent a significant gas load after some months of use. However, as previously discussed, its $H_{2,eq} \eta'_{ph}$ does not vary much for the coverages that the cold mass is expected to reach (see Table III). Therefore, a point in which the decaying rate of the $n_{H_{2,eq}}$ along dose is reversed, and the 100 h lifetime limit is surpassed due to high gas recycling taking place, is not expected to happen during 2 years of continuous operation. The ultimate gas density will be limited by this effect. For baseline beam parameters, it would be difficult to go under 1×10^{-9} mbar in the presented pessimistic scenario. Future measurements of η'_{ph} , with a lower ϵ_c value than the one corresponding to the used data, will allow to lower this estimated value.

Table X shows the calculated gas load ratio of each studied effect respect to the total one. Being both PSD and PSD' conservatively overestimated, the error with respect to the real phenomena may be large. Even so, the shown data are useful in an indicative way, highlighting PSD as the effect with the highest impact on the beam lifetime.

TABLE XI. Gas composition ratios of the main four species, for an arbitrary dose of 120 Ah.

Gas	H_2	CO	CO_2	CH_4
Total $H_{2,eq}$	29%	57%	12%	2%
Absolute	79%	17%	2%	1%
Abs w/o recycling	63%	31%	4%	2%

On the right side of Fig. 12 the $n_{H_{2,eq}}$ profile along the most irradiated MBs of the cell is plotted. The first two MB after the SSS would have lower gas density because the negligible SR emission from the SSS magnets. A gas density bump can be appreciated on the right side. It is ascribed to the absence of pumping in the interconnect region, to the high SR power density on the photon absorber present at the end of each MB, and to the high ESD gas load in this region. Along each magnet the gas density does not vary considerably thanks to the distributed cryopumping.

The calculated gas composition is shown in Table XI. In absolute units, H_2 is the predominant species. Nevertheless, after converting all the species to $H_{2,eq}$ units, CO becomes clearly the most relevant one, featuring the highest impact on the beam lifetime. Even if CO_2 presents the highest cross section, its η_{ph} is expected to be considerably low at the studied range of temperatures due to the chemical nature of this species.

V. CONCLUSIONS

In this paper the beam induced vacuum effects in the vacuum chamber of the FCC-hh have been studied. It is concluded that, in spite of the much higher synchrotron radiation power and beam screen temperature, the vacuum system of the FCC-hh shall be adequate.

The amount of conditioning which is needed to run the collider with baseline beam parameters and 100 h of beam-gas scattering lifetime is acceptable, i.e., lower than 80 Ah. These favorable provisions would be possible on one side thanks to the new beam screen design, which features a pumping speed more than three times higher than that of the LHC beam screen, and on the other one thanks to the expected SEY mitigation, relegating ESD to a minor role.

That being said, the high uncertainty of these estimations derived from the lack of data in the literature leaves these results as mere tentative. To completely assess the viability of the FCC-hh vacuum system, dedicated experiments will have to be carried out in the future.

ACKNOWLEDGMENTS

The authors would like to thank R. Cimino and the LNF-INFN team for the collaboration arranged to study the reflectivity and photoelectron yield of the beam screen materials and for sharing the data in advance to carry out

the study. The authors also acknowledge L. A. Gonzalez for the tests of the beam screen prototypes at BESTEX. This work was supported by the European Union's Horizon 2020 research and innovation programme under Grant No. 654305.

-
- [1] M. Benedikt, European Circular Energy Frontier Collider Study, H2020-INFRADEV-1-2014-1, proposal No. 654305, 2014.
- [2] M. Benedikt, M. C. Garrido, F. Cerutti, B. Goddard, J. Gutleber, J. M. Jimenez, M. Mangano, V. Mertens, J. A. Osborne, T. Otto, J. Poole, W. Riegler, D. Schulte, L. J. Tavian, D. Tommasini, and F. Zimmermann, Future Circular Collider, Tech. Rep. CERN-ACC-2018-0058 (CERN, Geneva, 2018), Volume 3—The Hadron Collider (FCC-hh), <https://cds.cern.ch/record/2651300>.
- [3] V. Baglin, G. Bregliozzi, J. M. Jimenez, and G. Lanza, Synchrotron radiation in the LHC vacuum system, in *Proceedings of the 2nd International Particle Accelerator Conference, San Sebastián, Spain* (EPS-AG, 2011), Vol. C110904, pp. 1563–1565.
- [4] A. Hofmann, Characteristics of synchrotron radiation, in CERN Accelerator School (CAS): Synchrotron Radiation and Free Electron Lasers, CERN Report No. CERN-LEP-DI-89-55, 1989, pp. 115–141, <http://cds.cern.ch/record/202177>.
- [5] O. Gröbner, Overview of the LHC vacuum system, *Vacuum* **60**, 25 (2001).
- [6] J. Gómez-Goñi, O. Gröbner, and A. G. Mathewson, Comparison of photodesorption yields using synchrotron radiation of low critical energies for stainless steel, copper, and electrodeposited copper surfaces, *J. Vacuum Sci. Technol. A* **12**, 1714 (1994).
- [7] I. Bellafont, M. Morrone, L. Mether, J. Fernández, R. Kersevan, C. Garion, V. Baglin, P. Chiggiato, and F. Pérez, Design of the future circular hadron collider beam vacuum chamber, *Phys. Rev. Accel. Beams* **23**, 033201 (2020).
- [8] P. Lebrun and L. Tavian, Beyond the Large Hadron Collider: A First Look at Cryogenics for CERN Future Circular Colliders, *Phys. Procedia* **67**, 768 (2015).
- [9] J. Chubb and I. Pollard, Experimental studies of hydrogen condensation on to liquid helium cooled surfaces, *Vacuum* **15**, 491 (1965).
- [10] O. Gröbner, The LHC vacuum system, in *Proceedings of the 1997 Particle Accelerator Conference, Vancouver, Canada* (1997), Vol. 3, pp. 3542–3546, <http://cds.cern.ch/record/356437>.
- [11] F. Pérez, P. Chiggiato, C. Garion, and J. Fernández, Preliminary beam screen and beam pipe engineering design, Technical Report No. EuroCirCol-P2-WP4-D4.3, 2017.
- [12] R. Valizadeh, O. B. Malyshev, S. Wang, T. Sian, M. D. Cropper, and N. Sykes, Reduction of secondary electron yield for E-cloud mitigation by laser ablation surface engineering, *Appl. Surf. Sci.* **404**, 370 (2017).
- [13] R. Valizadeh, O. B. Malyshev, S. Wang, S. A. Zolotovskaya, W. A. Gillespie, and A. Abdolvand, Low secondary electron yield engineered surface for electron cloud mitigation, *Appl. Phys. Lett.* **105**, 231605 (2014).
- [14] G. Tang, A. C. Hourd, and A. Abdolvand, Nanosecond pulsed laser blackening of copper, *Appl. Phys. Lett.* **101**, 231902 (2012).
- [15] P. C. Pinto, S. Calatroni, H. Neupert, D. Letant-Delrieux, P. Edwards, P. Chiggiato, M. Taborelli, W. Vollenberg, C. Yin-Vallgren, J. Colaux, and S. Lucas, Carbon coatings with low secondary electron yield, *Vacuum* **98**, 29 (2013).
- [16] C. Yin Vallgren, G. Arduini, J. Bauche, S. Calatroni, P. Chiggiato, K. Cornelis, P. Costa-Pinto, B. Henrist, E. Metral, H. Neupert, G. Rumolo, E. Shaposhnikova, and M. Taborelli, Amorphous carbon coatings for the mitigation of electron cloud in the CERN Super Proton Synchrotron, *Phys. Rev. Accel. Beams* **14**, 071001 (2011).
- [17] S. Calatroni, E. Garcia-Tabares, H. Neupert, V. Nistor, A. T. Pérez, M. Taborelli, P. Chiggiato, O. B. Malyshev, R. Valizadeh, S. Wackerow, S. A. Zolotovskaya, W. A. Gillespie, and A. Abdolvand, First accelerator test of vacuum components with laser-engineered surfaces for electron-cloud mitigation, *Phys. Rev. Accel. Beams* **20**, 113201 (2017).
- [18] R. Valizadeh, A. Hannah, J. Much, D. Whitehead, P. Krkotic, O. B. Malyshev, J. M. O'Callaghan, and M. Pont, Evaluation of LASER ablated surface engineering of copper and stainless steel for particle accelerators, Presentation in FCC Week 2019 (2019), <https://indico.cern.ch/event/727555/contributions/3468921/>.
- [19] L. A. Gonzalez, V. Baglin, I. Bellafont, S. Casalbuoni, P. Chiggiato, C. Garion, E. Huttel, R. Kersevan, and F. Pérez, Photodesorption Studies on FCC-hh Beam Screen Prototypes at KARA, Presentation in FCC Week 2019 (2019), <https://indico.cern.ch/event/727555/contributions/3447250/>.
- [20] L. Spallino, M. Angelucci, R. Larciprete, and R. Cimino, On the compatibility of porous surfaces with cryogenic vacuum in future high-energy particle accelerators, *Appl. Phys. Lett.* **114**, 153103 (2019).
- [21] V. Baglin, P. Chiggiato, and C. Garion, Vacuum System in The High Luminosity Large Hadron Collider, CERN, Geneva, 2020 (to be published).
- [22] L. A. Gonzalez, M. Gil-Costa, V. Baglin, P. Chiggiato, C. Garion, R. Kersevan, S. Casalbuoni, E. Huttel, I. Bellafont, and F. Pérez, Commissioning of a beam screen test bench experiment with a future circular hadron collider type synchrotron radiation beam, *Phys. Rev. Accel. Beams* **22**, 083201 (2019).
- [23] R. Kersevan, SYNRAD, a Montecarlo synchrotron radiation ray-tracing program, in *Proceedings of International Conference on Particle Accelerators* (IEEE, Washington D.C., 1993), pp. 3848–3850, https://accelconf.web.cern.ch/accelconf/p93/PDF/PAC1993_3848.PDF.
- [24] M. Ady and R. Kersevan, MOLFLOW+ and SYNRAD+ Website, (2018), <https://molflow.web.cern.ch/>.
- [25] M. Ady, Monte Carlo simulations of ultra high vacuum and synchrotron radiation for particle accelerators, Ph.D. thesis, Ecole Polytechnique, Lausanne, 2016, <https://cds.cern.ch/record/2157666>.
- [26] M. Ady and R. Kersevan, Introduction to the latest version of the test-particle monte carlo code molflow, in *Proceed-*

- ings of IPAC 2014* (JACoW, Dresden, 2014), pp. 2348–2350, <http://jacow.org/IPAC2014/papers/wepme038.pdf>.
- [27] S. Sgobba and G. Hochortler, A new non-magnetic stainless steel for very low temperature applications, in *Proceedings of the International Congress Stainless Steel 1999: Science and Market, Chia Laguna, Italy*, Vol. 2 (Associazione Italiana di Metallurgia, Milano, 1999), pp. 391–401.
- [28] R. Calder, O. Gröbner, A. G. Mathewson, V. V. Anashin, A. Dranichnikov, and O. B. Malyshev, Synchrotron radiation induced gas desorption from a Prototype Large Hadron Collider beam screen at cryogenic temperatures, *J. Vacuum Sci. Technol.* **14**, 2618 (1996).
- [29] C. Herbeaux, P. Marin, V. Baglin, and O. Gröbner, Photon stimulated desorption of an unbaked stainless steel chamber by 3.75 keV critical energy photons, *J. Vacuum Sci. Technol. A* **17**, 635 (1999).
- [30] O. Gröbner, Dynamic outgassing, CERN Technical Report No. CERN-OPEN-2000-275, 1999, <https://cds.cern.ch/record/455559>.
- [31] V. Anashin, A. Bulygin, O. Malyshev, L. Mironenko, E. Pyata, V. Volkov, and D. Kramer, Photodesorption and power testing of the SR crotch-absorber for BESSY-II, in *Proceedings of the 6th European Particle Accelerator Conference, Stockholm, Sweden* (1998), pp. 2163–2165, <https://cds.cern.ch/record/859323>.
- [32] L. A. Gonzalez, F. Pérez, I. Bellafont, V. Baglin, P. Chiggiato, C. Garion, R. Kersevan, S. Casalbuoni, and E. Huttel, Results on the FCC-hh beam screen sawtooth at the KIT electron storage ring KARA, in *Proceedings of IPAC 2019* (JACoW, Melbourne, 2019), pp. 1323–1326, <https://inspirehep.net/literature/1745028>.
- [33] V. Baglin, Measurement of the primary phodesorption yield at 4.2 K, 77 K and room temperature in a quasi-closed geometry, CERN Technical Report LHC Project Report 9, 1996, <https://cds.cern.ch/record/304957>.
- [34] O. S. Bruning, P. Collier, P. Lebrun, S. Myers, R. Ostojic, J. Poole, and P. Proudlock, LHC Design Report Vol. 1: The LHC Main Ring, CERN Technical Report No. 2004-003-V1, 2004, Chap. 12, https://edms.cern.ch/ui/file/445860/3/Vol_1_Chapter_12.pdf.
- [35] O. Gröbner, A. G. Mathewson, and P. C. Marin, Gas desorption from an oxygen free high conductivity copper vacuum chamber by synchrotron radiation photons, *J. Vacuum Sci. Technol. A* **12**, 846 (1994).
- [36] C. Foerster, H. Halama, G. Korn, M. Calderon, and W. Barletta, Desorption measurements of copper and copper alloys for PEP-II, *Vacuum* **44**, 489 (1993).
- [37] R. Cimino, M. Comisso, D. R. Grosso, T. Demma, V. Baglin, R. Flammini, and R. Larciprete, Nature of the Decrease of the Secondary-Electron Yield by Electron Bombardment and its Energy Dependence, *Phys. Rev. Lett.* **109**, 064801 (2012).
- [38] T. Kobari, M. Matumoto, S. Ueda, M. Kobayashi, and Y. Hori, Surface treatments and photodesorption of oxygen free copper used in an accelerator, in *Proceedings of International Conference on Particle Accelerators* (IEEE, Washington D.C., 1993), pp. 3903–3905, https://accelconf.web.cern.ch/accelconf/p93/PDF/PAC1993_3903.PDF.
- [39] V. Baglin, I. R. Collins, O. Gröbner, C. Grünhagel, and B. Jenninger, Molecular desorption by synchrotron radiation and sticking coefficient at cryogenic temperatures for H₂, CH₄, CO and CO₂, *Vacuum* **67**, 421 (2002).
- [40] M. Benedikt, D. Schulte, and F. Zimmermann, Optimizing integrated luminosity of future hadron colliders, *Phys. Rev. Accel. Beams* **18**, 101002 (2015).
- [41] V. V. Anashin, O. B. Malyshev, R. Calder, and O. Gröbner, A study of the photodesorption process for cryosorbed layers of H₂, CH₄, CO or CO₂ at various temperatures between 3 and 68 K, *Vacuum* **53**, 269 (1999).
- [42] O. Gröbner, VLHC Workshop, CERN, CERN-LHC/VAC, 2000.
- [43] V. Baglin, I. R. Collins, O. Gröbner, C. Grünhagel, and B. Jenninger, Synchrotron radiation studies of the lhc dipole beam screen with coldex, in *Proceedings of the 8th European Particle Accelerator Conference, Paris, 2002* (2002), pp. 2535–2537, <http://accelconf.web.cern.ch/Accelconf/e02/PAPERS/WEPDO09.pdf>.
- [44] O. B. Malyshev, V. V. Anashin, I. R. Collins, and O. Gröbner, Photon stimulated desorption processes including cracking of molecules in a vacuum chamber at cryogenic temperatures, CERN Technical Note 99-13, 1999.
- [45] V. Baglin and B. Jenninger, CERN Technical Report Coldex Run 24, 1999.
- [46] I. R. Collins and O. B. Malyshev, Dynamic gas density in the LHC interaction regions 1&5 and 2&8 for optics version 6.3, CERN Technical Report No. LHC-Project-Note-274, 2001, <http://cds.cern.ch/record/691797>.
- [47] F. Billard, N. Hilleret, and G. Vorlauffer, Some results on the electron induced desorption yield of OFHC copper, CERN Vacuum Technical Note 00-32, 2000.
- [48] E. La Francesca, A. Liedl, M. Angelucci, M. G. Sokolov, A. and Sertsu, F. Schäfers, F. Siewert, and R. Cimino, Study of reflectivity and photo yield on FCC-hh proposed beam screen surfaces, Poster in FCC Week 2018 (2018), <https://indico.cern.ch/event/656491/contributions/2938727/>.
- [49] A. Liedl, E. La Francesca, M. Angelucci, and R. Cimino, Photo reflectivity and photo electron yield of technical surfaces, e-Cloud Workshop, Isola d’Elba, Italy (2018), <https://agenda.infn.it/event/13351/contributions/18931/>.
- [50] E. La Francesca, A. Liedl, M. Angelucci, I. Bellafont, L. A. Gonzalez, L. Spallino, F. Siewert, M. G. Sertsu, A. Sokolov, F. Schäfers, and R. Cimino, Photo reflectivity and photo electron yield from copper technical surfaces (to be published).
- [51] G. Iadarola and G. Rumolo, PyECLOUD and build-up simulations at CERN, in *Proceedings of the Joint INFN-CERN-EuCARD-AccNet Workshop on Electron-Cloud Effects, La Biodola, Isola d’Elba, Italy, 2012* (2013), pp. 189–194, <https://doi.org/10.5170/CERN-2013-002.189>.
- [52] G. Iadarola, G. Rumolo, and G. Miano, Electron cloud studies for CERN particle accelerators and simulation code development, Ph.D. thesis, Università degli Studi di Napoli Federico II, 2014, <https://cds.cern.ch/record/1705520>.
- [53] V. V. Anashin, I. R. R. Collins, R. V. Dostovalov, N. V. Fedorov, O. Gröbner, A. Krasnov, O. B. Malyshev, and E. Pyata, Magnetic and electric field effects on the

- photoelectron emission from prototype LHC beam screen material, *Vacuum* **60**, 255 (2001).
- [54] F. Pérez, P. Chiggiato, O. B. Malyshev, R. Valizadeh, T. Sian, and R. Sirvinskaite, Proposal on surface engineering to mitigate electron cloud effects, Technical Report No. EuroCirCol-P2-WP4-M4.4, 2017.
- [55] A. Romano, G. Iadarola, K. Li, and G. Rumolo, Effect of the lhc beam screen baffle on the electron cloud buildup, in *Proceedings of IPAC 2016, Busan, Korea* (2016), pp. 1454–1457, <http://jacow.org/ipac2016/papers/tupmw016.pdf>.
- [56] O. B. Malyshev and A. Rossi, Ion desorption stability in the LHC, CERN Vacuum Technical Note 99-20, 1999.
- [57] O. B. Malyshev, The energy of the ions bombarding the vacuum chamber walls, CERN Technical Report No. Vacuum Technical Note 99-17, 1999.
- [58] O. B. Malyshev, The ion impact energy on the lhc vacuum chamber walls, in *Proceedings of the European Particle Accelerator Conference, Vienna* (EPS-IGA, Geneva, 2000), pp. 951–953, <https://accelconf.web.cern.ch/accelconf/e00/PAPERS/THP1B20.pdf>.
- [59] O. B. Malyshev, Ion induced pressure instability in the ILC positron DR, in *Proceedings of the International Particle Accelerator Conference, Kyoto, Japan* (2010), pp. 3566–3568, <https://accelconf.web.cern.ch/accelconf/IPAC10/papers/wepe093.pdf>.
- [60] M. Bassetti and G. A. Erskine, Closed expression for the electrical field of a two-dimensional Gaussian charge, CERN Technical Report No. CERN-ISR-TH-80-06, 1980, <http://cds.cern.ch/record/122227>.
- [61] F. F. Rieke and W. Prepejchal, Ionization cross sections of gaseous atoms and molecules for high-energy electrons and positrons, *Phys. Rev. A* **6**, 1507 (1972).